ChemComm

Chemical Communications

This article can be cited before page numbers have been issued, to do this please use: C. He, Z. Zhang and T. Li, *Chem. Commun.*, 2026, DOI: 10.1039/D6CC00741D.

ChemComm

View Article Online
DOI: 10.1039/D6CC00741D

COMMUNICATION

Interface-Induced Fast Li⁺ Transport In Mixed Ion–Electronic Conductor

Chenchen He,[a] Zhuoxun Zhang [a] and Tao Li [abc*]

Received 00th January 20xx,
Accepted 00th January 20xx

DOI: 10.1039/x0xx00000x

Interfacial instability between lithium metal and solid-state electrolytes limits the performance of all-solid-state lithium metal batteries (ASSLBs), leading to parasitic reactions, nonuniform Li^+ flux, and dendrite growth. Here, we develop a composite interlayer composed of anti-perovskite $Li_2OHCl_{0.75}Br_{0.25}$ (AP) and carbon nanotubes (CNT) to enhance both interfacial stability and ionic transport. The AP-CNT interlayer exhibits enhanced Li^+ conductivity arsing from interfacial electron transfer from AP to CNT, which generates a built-in electric field that facilitates Li^+ migration. Lithium symmetric cells incorporating this interlayer achieve a high critical current density of 2.4 mA cm^{-2} at 55 °C. This design integrates chemical robustness with coupled ion–electron transport, offering a generalizable strategy for safe, dendrite-free, and high-performance ASSLBs.

All-solid-state lithium metal batteries have emerged as promising candidates for next-generation electric vehicle energy storage. Their promise lies in solid-state electrolytes (SSEs), which offer high mechanical strength, single-ion (Li^+) conduction, and intrinsic non-flammability, enabling enhanced safety and the prospect of ultra-high energy density cycling[1, 2]. However, their practical implementation is severely hindered by unstable interfaces between SSEs and lithium metal anodes[3]. Owing to the strong reducing nature of lithium metal, spontaneous interfacial reaction occurs upon contact with SSEs, leading to the formation of a chemically and structurally heterogeneous interphase. In sulfide-based SSEs, such reduction produces ionically resistive decomposition products (e.g., Li_2S-, LiF-, and Li_3P-rich phases)[4, 5], which disrupt continuous Li^+ transport, induce non-uniform ion flux and local overpotential accumulation, and ultimately promote dendrite formation and cell failure[6]. To address these challenges, artificial interlayers—widely explored in metal electrodes and electrocatalysts,[7-9] have been introduced to chemically decouple the Li/SSE interface, preserve Li^+ transport continuity, and homogenize current distribution, thereby enhancing interfacial stability in ASSLBs[10, 11].

Pure ionic conductors are widely employed as artificial interlayers owing to their favourable chemical stability against Li metal; however, their low room-temperature Li^+ conductivity and high interfacial energy often result in severe interfacial polarization and inhomogeneous ion flux[12-14]. Anti-perovskite (AP) solid electrolytes exemplify this limitation. Shen et al. demonstrated that an AP interlayer at the Li/Li_3InCl_6 interface significantly improved chemical compatibility and current distribution, increasing the critical current density from 2.4 to 4.2 mA cm^{-2} and enabling stable Li plating/stripping for over 2400 h [15]. Nevertheless, the intrinsically low ionic conductivity of AP ($\approx 10^{-5}$ S cm^{-1} at room temperature) restricts Li^+ transport, typically requiring elevated temperatures (>80°C)[16], which compromises practical applicability and safety of SSBs.

In this context, mixed ionic-electronic conductor (MIEC) formed by incorporating conductive carbon into ionic conductors, offer a viable strategy to lower nucleation overpotential, alleviate interfacial polarization, and reduce lithium deposition behaviour[17]. However, most reported MIEC systems remain limited by insufficient ionic conductivity, resulting in aggravated polarization, and diminished control over lithium deposition during prolonged cycling[18, 19]. Therefore, preserving the intrinsic chemical stability of AP while enhancing Li^+ transport through rational composite design remains a key challenge for achieving uniform lithium deposition and long-term interfacial stability[20].

---

[a] Department of Chemistry, Virginia Tech, Blacksburg, VA, 24061 USA.
[b] Department of Chemistry and Biochemistry, Northern Illinois University, DeKalb, Illinois 60115, United States.
[c] X-ray Science Division, Argonne National Laboratory, Lemont, Illinois 60439, United States.

View Article Online
DOI: 10.1039/D6CC00741D

Here, we design and construct a composite interlayer composed of a $Li_2OHCl_{0.75}Br_{0.25}$ and carbon nanotubes to regulate coupled ionic and electronic transport at the lithium metal|sulfide solid electrolyte interface, thereby enhancing interfacial stability and electrochemical kinetics in all-solid-state lithium metal batteries. By systematically tuning the AP/CNT mass ratio (1-50 wt.% CNT), we identify a non-linear dependence of ionic conductivity on CNT content, with a maximum at 5 wt.% CNT, which preserves chemical stability while markedly enhancing Li^+ transport. Unlike previously reported MIEC interlayers that rely on enhanced electronic conductivity to reduce polarization[17, 21], our strategy exploits the work-function mismatch between AP and CNT to induce interfacial electron transfer until Fermi-level equilibration is achieved, resulting in charge redistribution and the establishment of a built-in electric field at the interface. This field converts boundary-limited transport in pristine AP into faster interfacial Li^+ migration (Fig. 1), representing a fundamentally different ion–electron coupling mechanism. As a result, the ionic conductivity of the composite interlayer is enhanced by more than tenfold relative to pristine AP, leading to substantially improved interfacial kinetics. Benefiting from these synergistic effects, Li symmetric cells incorporating the composite interlayer achieve a high critical current density of 2.4 mA cm^{-2} at 55°C. This work demonstrates a general design strategy for stabilizing lithium metal interfaces through synergistic ion-electron regulation.

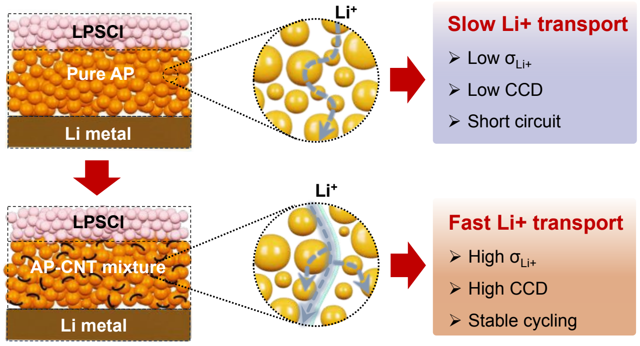

Fig. 1. Schematic illustration of Li^+ transport enhancement facilitated by the built-in electric field within the AP-CNT composite interlayer. While Li^+ transport in pure AP occurs along particle boundaries, the AP-CNT interface generates an internal electric field that accelerates Li^+ migration, creating highly efficient transport pathways.

The $Li_2OHCl_{0.75}Br_{0.25}$ SSE was synthesized following the procedure reported in Supplementary. AP–x% CNT composite (x = 1, 3, 5, 10, 50) was prepared by ball milling specific weight ratio of AP and CNT. High-resolution X-ray diffraction (XRD) (Figure S1, SI) shows the results of pure AP and its mixture with CNT. No new diffraction peaks were observed, except for additional peak at 7.88° corresponding to CNT, suggesting there is no structural change by mixing AP with CNT. The electronic conductivity of AP–CNT composites were measured at 55 °C using chronoamperometry (CA) method. The electronic conductivity increases monotonically with the CNT content. Once the CNT content exceeds 3 wt.%, the composite transitions into an electronic conductor (Figure S2, SI). Specifically, AP-5% CNT shows an electronic conductivity of 5.4 × 10^{-2} S·cm^{-1} (Figure S3, SI), which is more than eight orders of magnitude higher than that of pristine AP (1.27 × 10^{-10} S·cm^{-1}). Owing to their distinct electronic conductivity behaviours, the ionic conductivity of AP-x% CNT composites with low CNT content (x = 0, 1, 3) was evaluated using EIS, while samples with higher CNT content (x = 5, 10, 50) were characterized by the chronoamperometry method (Fig. 2a and b). Unlike electronic conductivity, the ionic conductivity displays a non-linear evolution, reaching a maximum of 1.41× 10^{-4} S·cm^{-1} at 5wt.% CNT, which is much higher than that of pristine AP (1.05 × 10^{-5} S·cm^{-1}), as shown in Fig. 2c. This behaviour is noteworthy, as ionic conductivity typically decreases with increased CNT content. These results are further supported by Tafel measurements. Figure 2d shows the Tafel curves of symmetric cells incorporating AP-CNT composite interlayers obtained at 55 °C. Consistent with the result of ionic conductivity, the AP-5%CNT interlayer exhibits the highest exchange current density of 0.02 mA cm^{-2}. The elevated exchange current density indicates accelerated interfacial kinetics and reduced energy barriers for Li^+ transfer, demonstrating that the composite interlayer facilitates efficient ion transport at the Li interface rather than merely improving electronic conductivity.

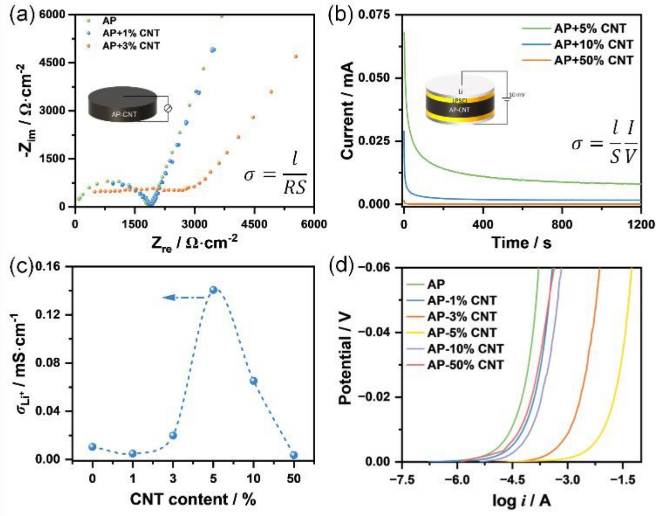

Fig. 2. (a) EIS profiles of SS/AP-x% CNT/SS (x=0, 1, 3) cells at 55 °C. (b) CA measurement of Li/LPSCl/AP-x% CNT/LPSCl/Li (x = 5, 10, 50) cell at 55 °C. The applied voltage is 10 mV. (c) Calculated ionic conductivity of AP-x% CNT from Fig. 2a, b. (d) Tafel curves of symmetric Li/AP−x% CNT/LPSCl/AP−x% CNT/Li (x % = 1, 3, 5, 10 and 50 wt %) cells at 55 °C.

To gain deeper insight into the mechanism underlying the enhanced ionic conductivity of AP–5% CNTs, Raman spectroscopy was carried out on AP–CNT composites by varying CNT contents. As shown in Fig. 3a and Figure S4, the samples containing CNTs exhibit a prominent D band at 1350 cm^{-1} and a G band at 1575 cm^{-1}, whereas pristine AP shows no significant Raman features. Quantitative analysis of the I_D/I_G ratio is presented in Fig. 3b. Pure CNTs display the lowest I_D/I_G ratio, consistent with their high graphitic order and minimal defect density. Upon mixing with AP, the I_D/I_G ratio increases and reaches a maximum at 5 wt.% CNT content, indicating the introduction of additional structural disorder within the CNTs. This enhanced defect density likely originates from perturbation of the sp^2 carbon network caused by electronic interaction between CNTs and AP.

View Article Online
DOI: 10.1039/D6CC00741D

To validate this interfacial electronic interaction, the surface potential of the AP–CNT composites was further examined using Kelvin probe force microscopy (KPFM). Variations in the contact potential difference (CPD) directly reflect changes in surface potential, with the average CPD values extracted from line profile measurements. As shown in Fig. 3c and Figure S5, pristine AP exhibits an average CPD of 21 mV, whereas AP–1%, AP–5%, AP-10% CNT displays a substantially higher CPD of 63, 120 and 100 mV, respectively. The non-monotonic variation of CPD with CNT content, with a maximum at 5 wt.% CNT, suggests that the surface potential change is not solely determined by the intrinsic work-function difference between AP and CNT, but instead reflects interfacial charge redistribution. As illustrated in Figure S6, the work-function mismatch drives electron transfer from CNT to AP until Fermi-level equilibration is achieved, leading to electron accumulation on the AP surface and the formation of positively charged vacancies on the CNT surface. This charge redistribution induces band bending in the AP phase and establishes a built-in electric field at the interface, as shown in Fig. 3d[22, 23]. Such a field provides an additional electrostatic driving force that alters the local potential energy landscape of Li$^+$. Thereby it effectively lowers the migration energy barrier and facilitates interfacial ion transport, accounting for the enhanced ionic conductivity observed in the AP–5% CNT system[22, 24].

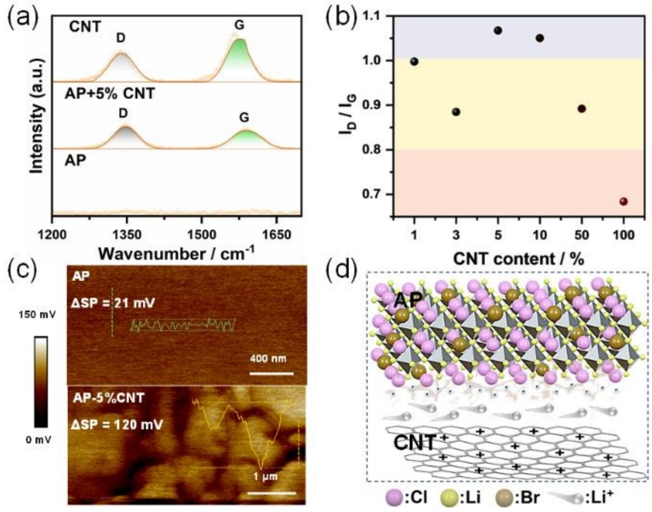

Fig. 3. (a) Raman spectra of AP, CNT and AP-5%CNT. (b) I_D/I_G ratios of AP–CNT composites with varying CNT contents (0%, 1%, 3%, 5%, 10%, 50%, and 100%). (c) KPFM images and contact potential differences of AP and AP-5%CNT. (d) Scheme of built in electric field.

The impact of AP–5% CNT interlayer on Li plating/stripping was investigated in Li/LPSCl/Li symmetric cells, in which LPSCl electrolyte was sandwiched between two AP or AP–5% CNT interlayers. The symmetric cells were charged and discharged at stepwise-increased current densities of 1h. As shown in Fig. 4a and 4b, the cell with the AP interlayer short-circuited immediately at a current density of 0.1 mA cm^{-2}, whereas the AP–5% CNT interlayer enabled a much higher critical current density of 2.4 mA cm^{-2}, demonstrating significantly enhanced interfacial stability. This value is also higher than that without an interlayer (Figure S7, SI). The effect of the interlayer was further evaluated in Li/LPSCl/AlO@NMC811 full cells with AP or AP-5% CNT interlayer at 55°C. For comparison, Li/LPSCl/AlO@NMC811 full cells without an interlayer were also assembled. The capacity of the Li/LPSC/LSO@NMC811 full cell without an interlayer rapidly decayed to 58.3 mAh g^{-1} after only 10 cycles (Figure S8, SI). This degradation arises from severe side reactions between the Li metal and the LPSCl electrolyte as well as the pore formation during Li metal stripping at low pressures due to the limited creep rate of the Li metal, which leads to increased polarization and suppressed capacity utilization[5, 25-28]. After adding an AP interlayer, the battery short-circuits even during the first charge cycle (Figure S9, SI). The failure is attributed to low ionic conductivity of AP, which readily promotes dendrite growth. Furthermore, the poor wettability (Figure S10, SI) between the AP and Li metal creates localized current hotspots, further accelerating non-uniform Li deposition and leading to rapid short-circuiting[29]. In contrast, the Li/LPSC/LSO@NMC811 full cell with AP-5% CNT exhibits superior performance, delivering a specific discharge capacity of 157.7 mAh g^{-1} in the first cycle and maintaining a discharge capacity of 134.0 mAh g^{-1} after 20 cycles. Fig. 4d highlights the advantages of the AP-CNT interlayer by comparing the cycling performance of solid-state batteries with and without the interlayer. This can be attributed to the multifunctional nature of the AP–CNT interlayer. On the one hand, the built-in electric field generated by the AP-5% CNT facilitates Li$^+$ migration across the interface. This interfacial effect effectively reduces ion transport resistance and ensures a more uniform Li$^+$ flux during cycling. Furthermore, the AP–CNT layer stabilizes lithium metal, mitigates detrimental side reactions between the lithium metal anode and the sulfide electrolyte, and withstands interfacial stress during repeated plating/stripping. Overall, these synergistic effects lead to slower capacity decay and higher discharge capacity retention in cells with AP–5% CNT interlayer.

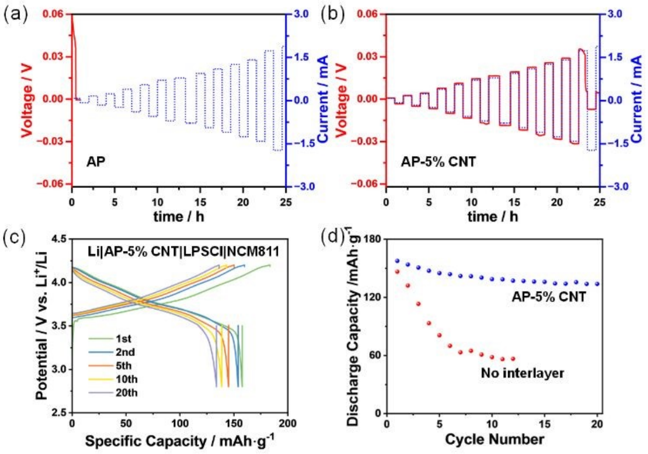

Fig 4. (a) Galvanostatic cycling of (a) Li/AP/LPSCl/AP/Li cell and (b) Li/AP-5%CNT/LPSCl/AP-5%CNT/Li cell at step-increased current densities at 55 °C. (c) Charge–discharge curves of the Li/AP-5%CNT/LPSCl/AlO@NCM811 cell at 55 °C. (d) Cycling performance of solid-state batteries with/without AP-CNT interlayer at a rate of 0.1C.

In summary, we have demonstrated a composite AP–CNT interlayer that simultaneously enhances interfacial stability and Li$^+$ transport in all-solid-state lithium-metal batteries. By incorporating a small fraction of CNTs into the anti-perovskite $Li_2OHCl_{0.75}Br_{0.25}$, interfacial electron transfer generates a built-in electric field, thereby facilitating Li⁺ migration and promoting a more homogeneous interfacial ion flux. As a result, the AP–5% CNT interlayer exhibits an ionic conductivity higher than that of pristine AP and enables stable lithium plating/stripping with a high critical current density of 2.4 mA cm^{-2} at 55 °C. When applied in full cells, this multifunctional interlayer markedly improves cycling stability and capacity retention by mitigating parasitic reactions, suppressing dendrite growth, and accommodating interfacial stress. Beyond this specific system, the concept of built-in electric fields to accelerate Li⁺ transport could be extended to anode and other solid-state electrolyte system, such as oxide- and polymer-based electrolytes,[30, 31] providing a general and effective strategy for designing high-performance, dendrite-free solid-state lithium-metal batteries.

We gratefully acknowledge the financial support from the Foundation for Vehicle Technologies Office of the Department of Energy of United States (Grant No. G2A25090). Use of the Advanced Photon Source and Center for Nanoscale Materials at Argonne National Laboratory was supported by the U. S. Department of Energy, Office of Science, Office of Basic Energy Sciences, under Contract No. DE-AC02-06CH11357.

Data availability

The data supporting this article have been included as part of the Supplementary Information. Supplementary information: XRD, chronoamperometry curves, Raman spectra, Galvanostatic cycling curves, Charge–discharge curves and further experimental details. See DOI: https://doi.org/DOI.

Conflicts of interest

There are no conflicts to declare.

Notes and references

1. E. P. Alsac, D. L. Nelson, S. G. Yoon, K. A. Cavallaro, C. Wang, S. E. Sandoval, U. D. Eze, W. J. Jeong and M. T. McDowell, *Chem. Rev.*, 2025, **125**, 2009-2119.
2. S. E. Sandoval, C. G. Haslam, B. S. Vishnugopi, D. W. Liao, J. S. Yoon, S. H. Park, Y. Wang, D. Mitlin, K. B. Hatzell, D. J. Siegel, P. P. Mukherjee, N. P. Dasgupta, J. Sakamoto and M. T. McDowell, *Nat. Mater.*, 2025, **24**, 673-681.
3. W. D. Richards, L. J. Miara, Y. Wang, J. C. Kim and G. Ceder, *Chem. Mater.*, 2015, **28**, 266-273.
4. T. Swamy, X. Chen and Y.-M. Chiang, *Chem. Mater.*, 2019, **31**, 707-713.
5. D. H. S. Tan, E. A. Wu, H. Nguyen, Z. Chen, M. A. T. Marple, J.-M. Doux, X. Wang, H. Yang, A. Banerjee and Y. S. Meng, *ACS Energy Letters*, 2019, **4**, 2418-2427.
6. M. Zhou, Y. Liao, L. Li, R. Xiong, G. Shen, Y. Chen, T. Huang, M. Li, H. Zhou and Y. Zhang, *Journal of Energy Chemistry*, 2023, **85**, 181-190.
7. H. Chen, C. Meng, Z. Jiao, A. Yuan and H. Zhou, *Energy Fuels*, 2025, **39**, 4069-4078.
8. S. Qiang, J. Chen, S. Huang, H. Xu, X. Zhuo, H. Zhou, A. Yuan, H. Zhou and Y. Qiao, *J. Colloid Interface Sci.*, 2026, **701**, 138722.
9. Z. Zhao, J. Chen, H. Zhou, B. Hu, C. Meng, A. Yuan and Y. Qiao, *Metals Advances*, 2026, **40**, 62-70.
10. Y. Su, L. Ye, W. Fitzhugh, Y. Wang, E. Gil-González, I. Kim and X. Li, *Energy Environ. Sci.*, 2020, **13**, 908-916.
11. P. Ren, X. Wang, B. Huang, Z. Liu and R. Liu, *Journal of Energy Storage*, 2024, **82**.
12. X. Fan, X. Ji, F. Han, J. Yue, J. Chen, L. Chen, T. Deng, J. Jiang and C. Wang, *Sci Adv*, 2018, **4**, eaau9245.
13. J. Su, M. Pasta, Z. Ning, X. Gao, P. G. Bruce and C. R. M. Grovenor, *Energy Environ. Sci.*, 2022, **15**, 3805-3814.
14. R. Guo, K. Zhang, W. Zhao, Z. Hu, S. Li, Y. Zhong, R. Yang, X. Wang, J. Wang, C. Wu and Y. Bai, *Energy Mater. Adv.*, 2023, **4**.
15. L. Shen, Z. Wang, S. Xu, H. M. Law, Y. Zhou and F. Ciucci, *Nat. Commun.*, 2025, **16**, 3687.
16. Z. D. Hood, H. Wang, A. Samuthira Pandian, J. K. Keum and C. Liang, *J. Am. Chem. Soc.*, 2016, **138**, 1768-1771.
17. Z. Wang, J. Xia, X. Ji, Y. Liu, J. Zhang, X. He, W. Zhang, H. Wan and C. Wang, *Nat. Energy*, 2024, **9**, 251-262.
18. S.-Q. Li, Z. Wang, Z. Sun, X. Zheng, F.-H. Du, J.-N. Yang, Y.-W. Zhang, Y. Sun, H. Zong, M.-L. Guo, X.-Y. Wu, Y. Xu, G. Wang, C. Wu, Q. Zhang and K.-X. Wang, *ACS Energy Letters*, 2025, **10**, 5972-5981.
19. R. Xu, F. Han, X. Ji, X. Fan, J. Tu and C. Wang, *Nano Energy*, 2018, **53**, 958-966.
20. Y. Zhao and L. L. Daemen, *J. Am. Chem. Soc.*, 2012, **134**, 15042-15047.
21. C. Yang, L. Zhang, B. Liu, S. Xu, T. Hamann, D. McOwen, J. Dai, W. Luo, Y. Gong, E. D. Wachsman and L. Hu, *Proc. Natl. Acad. Sci. U. S. A.*, 2018, **115**, 3770-3775.
22. L. Du, Y. Zhang, Y. Xiao, D. Yuan, M. Yao and Y. Zhang, *Energy Environ. Sci.*, 2025, **18**, 2949-2961.
23. G. Xiao, K. Yang, Y. Qiu, P. Shi, G. Zhong, X. An, Y. Ma, L. Chen, S. Guo, J. Mi, Z. Han, T. Hou, H. Yan, Y. Tian, X. Zhang, Y. Cao, M. Liu, Z. Zhou and Y. B. He, *Adv. Mater.*, 2025, DOI: 10.1002/adma.202415411, e2415411.
24. M. Yang, K. Yang, Y. Wu, Z. Wang, T. Ma, D. Wu, L. Yang, J. Xu, P. Lu, J. Peng, Z. Jiang, X. Zhu, Q. Gao, F. Xu, L. Chen, H. Li and F. Wu, *ACS Nano*, 2024, **18**, 16842-16852.
25. S. Wenzel, S. J. Sedlmaier, C. Dietrich, W. G. Zeier and J. Janek, *Solid State Ionics*, 2018, **318**, 102-112.
26. J. M. Doux, H. Nguyen, D. H. S. Tan, A. Banerjee, X. Wang, E. A. Wu, C. Jo, H. Yang and Y. S. Meng, *Adv. Energy Mater.*, 2019, **10**, 1903253.
27. C. Wang, Y. Liu, W. J. Jeong, T. Chen, M. Lu, D. L. Nelson, E. P. Alsac, S. G. Yoon, K. A. Cavallaro, S. Das, D. Majumdar, R. Gopalaswamy, S. Xia and M. T. McDowell, *Nat. Mater.*, 2025, **24**, 907–916.
28. L. Di, Z. Huang, L. Gao, Y. Zuo, J. Zhu, M. Sun, S. Zhao, J. Zheng, S. Han and R. Zou, *Sci Adv*, 2025, **11**, eadw9590.
29. G. Cen, H. Yu, R. Xiao, L. Ben, R. Qiao, J. Zhu, X. Zhang, G. Liu, K. Jiang, X. Yao, H. Zhang and X. Huang, *Nat. Sustain*, 2025, **8**, 1360-1370.
30. M. Liu, W. Xu, S. Liu, B. Liu, Y. Gao and B. Wang, *Adv Sci (Weinh)*, 2024, **11**, e2402915.
31. J. Kondo, Y. Iga, K. Otani, R. Noba, H. Hikosaka, Y. Kondo, Y. Katayama and Y. Yamada, *The Journal of Physical Chemistry C*, 2025, **129**, 15231-15238.

View Article Online
DOI: 10.1039/D6CC00741D

Data availability

The data supporting this article have been included as part of the Supplementary Information. Supplementary information: XRD, chronoamperometry curves, Raman spectra, Galvanostatic cycling curves, Charge–discharge curves and further experimental details. See DOI: https://doi.org/DOI.